RSC Advances

PAPER

View Article Online
View Journal | View Issue

Cite this: *RSC Adv.*, 2025, **15**, 33443

Methodological insights into sulfur immobilization techniques on commercial carbon for lithium–sulfur batteries

Yelena Shinkarova,[a] Malika Tursynbek,[a] Mukhammed Kenzhebek,[bcd] Batukhan Tatykayev,[c] Zhazira Supiyeva,[de] Temirlan Kerimkul,[ad] Fail Sultanov*[bcd] and Almagul Mentbayeva *[b]

Lithium–sulfur batteries (LSBs) are considered as some of the most promising next-generation energy storage systems due to their high theoretical capacity and energy density. However, their practical application is hindered by challenges such as the shuttle effect, low conductivity of sulfur, and volume changes during cycling. A key factor to address these issues is the strategy used to incorporate sulfur into the carbon host, which significantly affects the cathode structure and electrochemical performance. In this study, we compare four distinct sulfur immobilization strategies – chemical precipitation (ChP), ball milling infiltration (BM), dissolution-crystallization (DC), and melt diffusion (MD) – using acetylene black (AB) as a conventional conductive carbon host. Each method yields AB@S composites with varying sulfur distributions, loading efficiencies, and interfacial characteristics. Comprehensive morphological and electrochemical characterization, including thermogravimetric analysis (TGA), scanning electron microscopy (SEM), and X-ray diffraction (XRD), confirms differences in sulfur content, particle morphology, and crystalline structure depending on the infiltration route. Electrochemical testing reveals that the synthesis approach is critical in determining the redox kinetics, reversibility, and cycling stability of Li–S batteries. Among the tested approaches, the AB@S cathode fabricated *via* the BM method delivers the most balanced performance, showing a comparatively high initial discharge capacity of 816 mAh g^{-1} at 0.1C, improved coulombic efficiency, and enhanced long-term cycling stability, retaining 68% of capacity, unlike DC and MD (about 60%) and ChP (55%) cells.

Received 5th August 2025
Accepted 8th September 2025

DOI: 10.1039/d5ra05694b

rsc.li/rsc-advances

1 Introduction

The growing demand for electric vehicles (EVs) and renewable energy systems, and the rapid spread of various portable devices, require engineers to develop and advance new battery technologies.[1–4] Despite their efficiency, modern lithium-ion batteries (LIBs) are constrained by limited energy density and service life, making them insufficient to meet the rapidly growing energy demands of society in the near future. Consequently, researchers are actively exploring novel chemical processes and advanced materials aimed at significantly enhancing battery performance. Among the most promising alternatives for next-generation energy storage are lithium–sulfur (Li–S) batteries, owing to their high theoretical energy density and cost-effectiveness. With a high theoretical discharge capacity of 1675 mAh g^{-1} and an energy density of 2600 Wh kg^{-1}, Li–S batteries significantly outperform conventional LIBs, making them strong candidates for the development of next-generation high-energy storage systems.

However, the complex electrochemical processes in Li–S batteries pose significant challenges for practical application and commercialization. While sulfur is widely available, non-toxic, and cost-effective, it has an insulating nature, which limits its ability to function as an electrode material and effectively conduct electric current. Problems with Li–S batteries also include low cycle life due to dissolution of lithium polysulfides (LiPSs) known as the shuttle effect,[5–8] electrolyte compatibility issues,[9,10] and volume expansion during discharge, which in turn leads to damage to the electrode and rapid fading of capacity.[11–13] Various strategies have been explored to overcome these limitations, including developing a suitable sulfur host material, separator modification, use of highly effective binders, lithium anode protection, the investigation of alternative absorption agents, and electrolytes.[14–18] Among various

[a]*Institute of Batteries LLC, Kabanbay Batyr Ave. 53, Astana, 010000, Kazakhstan*
[b]*Department of Chemical and Materials Engineering, School of Engineering and Digital Sciences, Nazarbayev University, Kabanbay Batyr Ave. 53, Astana, 010000, Kazakhstan. E-mail: fail.sultanov@nu.edu.kz; almagul.mentbayeva@nu.edu.kz*
[c]*National Laboratory Astana, Nazarbayev University, Kabanbay Batyr Ave. 53, Astana, 010000, Kazakhstan*
[d]*Satbayev University, Almaty, 050013, Kazakhstan*
[e]*Faculty of Chemistry and Chemical Technology, al-Farabi Kazakh National University, 71 Al-Farabi Ave, Almaty, 050013, Kazakhstan*

components, particular attention is focused on the development of efficient cathode materials. A well-designed host structure can enhance sulfur utilization, improve electrical conductivity, suppress polysulfide dissolution, and mitigate volume expansion, ultimately leading to improved cycling stability and electrochemical performance.

Among the various classes of sulfur host materials investigated for Li–S batteries, prominent examples include metal–organic frameworks (MOFs),[19,20] metal oxides (*e.g.*, TiO_2, Fe_2O_3, MnO_2),[21–23] metal sulfides (*e.g.*, MoS_2, CoS_2),[24–27] conducting polymers (*e.g.*, polyaniline, polypyrrole),[28–31] and Mxenes.[32,33] However, despite this broad range of options, the majority of research efforts have focused on carbon–sulfur composites. Carbon-based materials such as graphite, carbon nanotubes, graphene, carbon-based aerogels, and various types of porous carbon are widely employed as sulfur hosts due to their high electrical conductivity, tunable porosity, and chemical stability.[34–40] These carbon matrices not only facilitate the transport of electrons and lithium ions but also help mitigate the dissolution of polysulfides through physical confinement and chemical interactions. Nevertheless, the electrochemical performance of sulfur–carbon cathodes is influenced not only by the choice of host material but also critically by the method of sulfur immobilization. The selected synthesis technique determines the dispersion of sulfur, the nature of its interaction with the carbon framework, and the structural integrity during cycling, all of which significantly impact the overall battery performance. As a result, the development and comparative evaluation of different sulfur incorporation strategies remain a key area of interest. Advances in materials science and electrochemical engineering have enabled a wide range of sulfur loading techniques, including mechanochemical synthesis *via* ball milling, melt diffusion, supercritical fluid impregnation, vacuum blending, chemical deposition, solution-based crystallization, electrodeposition, and more specialized methods such as microemulsion templating and sulfate-mediated precipitation.[41] Among these, four widely adopted and representative methods are: chemical precipitation (ChP), ball milling (BM), dissolution-crystallization (DC), and melt diffusion (MD). These techniques differ significantly in terms of sulfur distribution, composite microstructure, and resultant electrochemical behavior, warranting systematic investigation and comparison.

The ChP method typically involves dispersing the carbon matrix in deionized water or a surfactant medium, such as cetyltrimethylammonium bromide (CTAB), or reacting it with sulfur precursors (*e.g.*, sodium thiosulfate) in the presence of strong acids like HCl or H_2SO_4. Sulfur is precipitated *in situ* onto the carbon matrix, followed by filtration and drying. This method is known for providing fine sulfur dispersion and good interfacial contact. For instance, Wang *et al.*[42] achieved an initial discharge capacity of 1232.5 mAh g^{-1}, which decreased to 800 mAh g^{-1} after 50 cycles. Sun *et al.*[43] reported 1257 mAh g^{-1} for a ternary polyaniline/sulfur/acetylene black (AB) composite, though capacity declined to 600 mAh g^{-1} over 100 cycles. Similarly, Li *et al.*[44] attained a uniform nanoscale sulfur distribution on AB, but the specific capacity fell from 925 mAh g^{-1} to 361 mAh g^{-1} at 100 cycles. These results highlight ChP's potential for homogeneous sulfur dispersion, but also its tendency toward capacity fading, likely due to polysulfide dissolution and poor long-term confinement.

In contrast, the BM method allows for the preparation of sulfur–carbon composites by mechanically blending the materials at high speeds (typically 300–500 rpm), which makes it scalable and cost-effective. This technique offers simplicity and uniform particle mixing, although it may not ensure deep sulfur infiltration or chemical bonding. Li *et al.*[45] achieved 612.9 mAh g^{-1} using S/Super-P composites, while Kaiser *et al.*[46] demonstrated capacities of 1200 and 1172 mAh g^{-1} for ball-milled carbon black and activated carbon composites, respectively. Xu *et al.*[47] obtained 1265.3 mAh g^{-1} with graphite-based composites. However, capacity fading and poor sulfur confinement over long cycles are recurring challenges with this method.

The DC infiltration method involves dissolving sulfur in carbon disulfide (CS_2), followed by mixing with carbon and heat treatment at 155 °C for sulfur impregnation, then annealing at 200 °C under inert gas. This multi-step approach offers improved sulfur confinement due to recrystallization within carbon pores. Zhang *et al.*[48] demonstrated an initial capacity of 1015 mAh g^{-1} with good reversibility (908 mAh g^{-1} after 100 cycles), indicating the effectiveness of this method in controlling active material loss.

MD remains the most widely used approach due to its simplicity and efficacy. It involves heating sulfur and carbon at 150–160 °C, allowing molten sulfur to infiltrate the porous framework. Chen *et al.*[49] employed MD to synthesize ordered mesoporous carbon/sulfur composites, achieving 1138 mAh g^{-1} at 0.5C with stable cycling for over 400 cycles. Despite its advantages, MD often lacks precise control over sulfur particle size and distribution, potentially leading to uneven electrochemical activity and sulfur migration.

Although these methods have been extensively explored, a clear scientific gap remains. In most reported studies, the focus is placed on tailoring host materials, while sulfur immobilization is usually performed by a single, arbitrarily chosen technique. Moreover, many comparative works differ in host type, sulfur content, or testing protocols, or remain limited to review-style theoretical discussions without systematic experimental benchmarking.[37,41,50–59] Only a few studies have attempted direct comparisons of immobilization techniques, but their findings remain inconsistent. For instance, Jiao *et al.*[60] compared ChP and MD, Geng *et al.*[61] reported superior performance of ChP over BM, and Park *et al.*[62] demonstrated the advantage of DC over MD. Zhang *et al.*[56] further investigated three infiltration routes using hierarchical porous carbon and observed notable differences in sulfur distribution and cycling stability, while Bonilla *et al.*[63] concluded that MD is preferable for highly porous carbons. These comparative studies often differ in key variables such as the type of carbon used (carbon nanotubes, mesoporous carbon, graphene), synthesis parameters (temperature, time, sulfur content), and electrochemical testing protocols. Such inconsistencies hinder accurate assessment and limit reproducibility. This lack of standardization

creates confusion and hinders rational selection of synthesis strategies for practical Li–S batteries development.

To address this critical gap, our study systematically compares ChP, BM, DC, and MD methods for sulfur immobilization using a standardized approach. We deliberately selected AB as a model host material because it is commercially available, and commonly employed in Li–S research, thereby minimizing variability related to host structure or surface chemistry. By applying identical sulfur loading ratios (target 70 wt%), optimized synthesis conditions, and testing protocols, this work isolates the impact of the immobilization technique itself on sulfur dispersion, pore infiltration, and electrochemical behavior.

Our comparative evaluation reveals that, among the four investigated techniques, the BM method provides the most balanced electrochemical performance and synthesis efficiency. Specifically, the BM composite shows the most homogeneous sulfur distribution, and stronger sulfur confinement compared to composites of the other three methods. Electrochemical testing further supports good redox reversibility and peak stability of the BM electrode over repeated cycles. Besides, the BM cell possesses the lowest charge-transfer resistance ($R_{ct} \approx 26\ \Omega$) and the highest Li^+ diffusion coefficient ($1.39 \times 10^{-11}\ cm^2\ s^{-1}$), correlating with its stable cycling. The BM cell also delivers an initial discharge capacity of 816 mAh g^{-1} at 0.1C with 68% retention after 100 cycles, maintaining nearly 99% coulombic efficiency. The data validate the BM method as a superior synthesis technique for producing high-performance Li–S cathodes.

2 Materials and methods

2.1 Chemicals

Sulfur powder (S, ≥99.0%), sodium thiosulfate ($Na_2S_2O_3$), and carbon disulfide (CS_2 anhydrous, ≥99.0%) were purchased from Sigma-Aldrich. Conductive AB was purchased from the MTI group. Argon (Ar (99.993%)) was purchased from Ikhsan Gas Company. Ultrapure deionized (DI) water was used in all experiments. All chemicals were used without further purification.

2.2 Preparation of AB@S cathode material

Sulfur was immobilized into AB using four conventional synthesis approaches – chemical precipitation (ChP), ball milling (BM), dissolution-crystallization (DC), and melt diffusion (MD). For all methods, a fixed sulfur-to-carbon weight ratio of 7 : 3 was maintained to ensure consistency in comparative analysis.

2.2.1 AB@S cathode material preparation *via* ChP method. The AB@S composite preparation *via* ChP involved the use of AB and sodium thiosulfate ($Na_2S_2O_3$) as starting materials. The powder material masses were adjusted to achieve a composite with a sulfur content of 70 wt%. Therefore, AB (0.16 g) was dispersed in 2-propanol (150 mL) to create a stable suspension. The mixture was stirred vigorously, ensuring uniform dispersion of the carbon particles. $Na_2S_2O_3$ (5.33 g) was dissolved in DI water (200 mL) to form an aqueous solution. Then, the AB suspension was gradually added to the $Na_2S_2O_3$ solution under continuous stirring. Afterward, 1 M hydrochloric acid (HCl, 2.5 mL) was added dropwise to the mixture to initiate a chemical reaction and precipitate sulfur onto carbon.[41] After the reaction was complete, the mixture was transferred to a centrifuge. The precipitated AB@S composite was separated from the acidic reaction medium by centrifuging at 3500 rpm for 5 minutes. The supernatant was discarded, and the remaining composite was dried in a vacuum oven at 60 °C for 12 hours to eliminate residual solvent and water.

2.2.2 AB@S cathode material preparation *via* BM method. The cathode material prepared *via* the BM method was obtained by initially mixing sulfur powder and AB in a mortar to ensure uniform pre-blending prior to mechanical processing. The premixed powder (1.0 g) was then transferred to a BM jar containing stainless steel milling balls with a ball-to-sample weight ratio of 40 : 1. Pure ethanol (5 mL) was subsequently added at the beginning as a process-control agent to promote uniform mixing and suppress particle agglomeration. High-energy BM was conducted at a rotational speed of 500 rpm for a total of 2 hours, applied as four 30-minute cycles, with intermediate rest intervals to mitigate overheating. Upon completion, the resulting composite was dried in an oven at 60 °C for 12 hours to evaporate residual ethanol. The dried material was then sieved to separate the composite powder from the balls.

2.2.3 AB@S cathode material preparation *via* DC method. To prepare a sulfur–AB composite containing 70 wt% by DC, 0.42 g of sulfur was dissolved in a mixture of CS_2 and isopropanol (IPA (7 : 3 mL)) under magnetic stirring. Simultaneously, 0.15 g of AB was suspended in IPA (using a sufficient volume to submerge the powder completely) and ultrasonicated with a probe sonicator for 20 minutes. Afterward, the prepared CS_2/IPA solution was poured into the AB suspension. The combined solution was stirred magnetically, followed by further ultrasonication in a bath sonicator until the CS_2/IPA solution completely evaporated. The mixture was then subjected to heat treatment in a tube furnace at 155 °C for 12 hours (heating rate of 10 °C per minute) in an Ar atmosphere, followed by a 1-hour annealing process at 200 °C for sulfur residue elimination from the surface.

2.2.4 AB@S cathode material preparation *via* MD method. The homogeneous mixture of commercial sulfur and AB was prepared by mechanical mixing in the agate mortar. To prevent oxidation and contamination, the mixture was placed into an autoclave, which was sealed under an Ar atmosphere inside a glovebox. The hermetic autoclave was heated in an oven at 155 °C for 15 hours, allowing the sulfur to melt and diffuse into the carbon matrix. After the heating process, the autoclave was removed and allowed to cool to room temperature before opening.[64] The resulting AB@S composite was collected for further use.

2.3 Sample characterization

To comprehensively analyze the properties of the synthesized materials, a suite of complementary characterization

techniques was employed. Surface morphology and microstructural features were examined using a scanning electron microscope (SEM) Crossbeam 540 equipped with energy-dispersive spectroscopy (EDS) and a JEOL JEM-1400 Plus transmission electron microscope (TEM), enabling visualization of particle distribution and nanoscale architecture. Crystalline structures and phase compositions were analyzed through X-ray diffraction (XRD) performed on the X-ray Diffraction System – SmartLab (Rigaku) using CuKα radiation ($k = 0.15418$ nm). Raman spectroscopy analysis was conducted with a Raman spectrometer (LabRAM, Horiba, 473 nm excitation wavelength). Thermogravimetric analysis (TGA) was conducted on a Simultaneous Thermal Analyzer (STA) 6000 in a nitrogen medium to assess thermal stability and sulfur content. Elemental analysis for carbon, hydrogen, nitrogen, and sulfur (CHNS) was performed using a Vario Macro Cube elemental analyzer. The specific surface area and pore size distribution were measured using a Nitrogen Porosimeter (Autosorb iQ Series) based on the Brunauer–Emmett–Teller (BET) method.

2.4 Electrochemical characterization

2.4.1 Cathode preparation. The cathode slurry was prepared by mixing AB@S composite, additional AB, and polyvinylidene fluoride (PVDF) binder in a weight ratio of 8 : 1 : 1. *N*-Methyl-2-pyrrolidone (NMP) was added as a solvent. The homogeneous slurry was then cast onto carbon-coated aluminum foil using the Doctor Blade technique. After coating, the cathodes were dried in a vacuum oven at 60 °C for 12 hours to remove residual solvent and ensure proper adhesion. The dried cathode was then punched into circular discs with a diameter of 15 mm. The sulfur loading in the cathodes was controlled to fall within the range of 1.0–1.13 mg cm^{-2}.

2.4.2 Coin cell assembly. CR-2032-type coin cells were assembled in an argon-filled glovebox to avoid contamination and degradation of the components. The assembly process involved several steps. Firstly, a 15 mm diameter cathode was placed onto the stainless steel base of the coin cell. The electrolyte used consisted of 1 M lithium bis(trifluoromethanesulfonyl)imide (LiTFSI) with 2 wt% lithium nitrate ($LiNO_3$) dissolved in a solvent mixture of 1,3-dioxolane (DOL) and 1,2-dimethoxyethane (DME) in a 1 : 1 v/v ratio. Approximately 20 μL of this electrolyte was dispensed onto the anode surface. Then, a 19 mm diameter polypropylene-based separator was positioned over the cathode. The separator was pre-wetted with the electrolyte to ensure good ionic contact. After that, a lithium metal disc of 16 mm diameter was placed on top of the separator as the anode. The components were covered with a stainless steel spacer and spring before sealing the coin cell using a hydraulic crimping machine.

2.4.3 Electrochemical testing. The electrochemical behavior of the assembled coin cells was investigated using cyclic voltammetry (CV). The CV measurements were conducted at a scan rate of 0.1 mV s^{-1} over a voltage range of 1.6–2.8 V *versus* Li/Li$^+$ using a VMP3 potentiostat/galvanostat (Bio-Logic Instruments). The coin cells also underwent galvanostatic charge–discharge tests using a Neware Battery Tester (BTS 7.5.4). These tests were conducted to evaluate the specific capacity, coulombic efficiency, and cycling stability of the cathodes. The EIS tests were performed using a VMP3 potentiostat/galvanostat over a frequency range of 100 kHz to 10 mHz with an amplitude of 5 mV to analyze the resistance contributions from the electrolyte, electrode interface, and charge transfer processes.

3 Results and discussion

3.1 Characterization of the AB@S cathode material obtained by different methods

The sulfur content in the AB@S composites was evaluated using TGA, with the results shown in Fig. 1a. A gradual mass loss was observed between 200–300 °C, corresponding to the evaporation of elemental sulfur. Beyond 300 °C, the mass remained stable for most samples, indicating complete sulfur removal. Notably, the composite prepared by the BM method exhibited continued sulfur loss up to ~340 °C. This delayed release is primarily attributed to the more homogeneous distribution of sulfur and its effective incorporation into fine pores of the carbon framework, which strengthens physical confinement and adsorption of sulfur species within the host.[65] Nevertheless, the possibility of structural changes induced by the mechanochemical process requires careful consideration. Previous work has demonstrated that even under harsher BM conditions (800 rpm, 12 h), no evidence of C–S bond formation between sulfur and AB was observed by XPS.[66] Since studies specifically on AB are limited, we also examined reports on other sulfur–carbon composites, which similarly indicated that high-energy BM does not result in stronger C–S interactions than those observed in composites prepared by other methods.[63] However, it cannot be fully excluded that, even at 500 rpm, the intensive mechanical forces might partially disrupt the cyclic S_8 structure and promote the formation of chain-like polysulfide species,[47] which could also contribute to the shifted sulfur volatilization temperature in the TGA profile. TGA also revealed that the initial sulfur loading in composites prepared by ChP and DC methods was significantly below the target of 70 wt%, equaling only 45 wt% and 59 wt%, respectively (Fig. S1), possibly due to inevitable sulfur loss during the processes frequently occurring in these methods.[61,62] To overcome this, the synthesis protocols were optimized through experimental calibration. For the DC method, a sulfur-to-carbon mass ratio of 7.4 : 2.6 was found to result in 70.4 wt% sulfur content. Similarly, for the ChP method, a sulfur-to-AB mass ratio of 9 : 1 was required to reach the same sulfur loading. These findings highlight a key limitation of both methods: achieving the desired sulfur content requires significant empirical adjustment, indicating poor stoichiometric predictability and limited control over sulfur incorporation. Additionally, CHNS elemental analysis (Table S1) confirmed the sulfur incorporation trends observed in the TGA results (pure AB exhibited a high carbon content of 98 wt%). After stoichiometric correction to achieve the target sulfur loading, the sulfur content in all composites ranged between the lowest 69.8 wt% for DC and the highest 74.5 wt% for ChP,

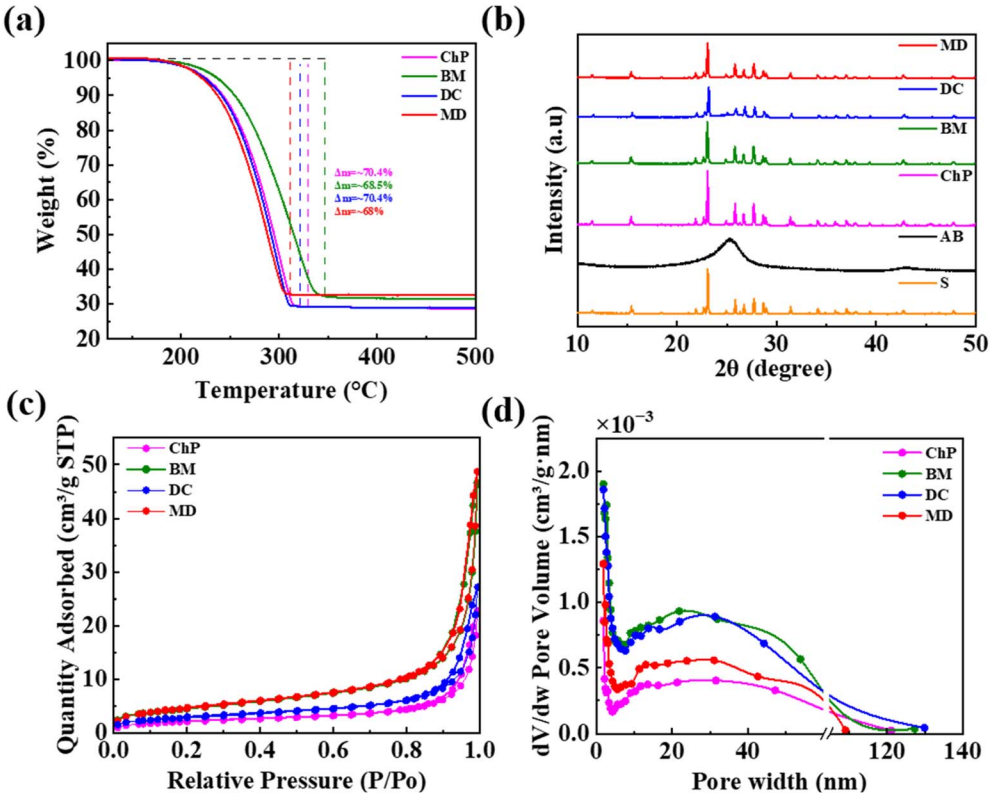

Fig. 1 (a) TGA results; (b) XRD patterns, (c) low temperature N_2 adsorption/desorption isotherms, and (d) pore size distribution for AB@S cathode materials synthesized *via* four different methods.

which is consistent with the TGA data, taking into account the measurement errors. In the AB@S composites, the carbon content ranged from 23.4 wt% to 30.2 wt%. Minor amounts of oxygen, hydrogen, and nitrogen were also detected, likely originating from precursor materials or surface functionalities introduced during synthesis.

The phase structure of elemental sulfur, AB, and sulfur–carbon composites (AB@S) synthesized *via* different immobilization methods was characterized by X-ray diffraction (XRD), as shown in Fig. 1b. All AB@S composites exhibit distinct diffraction peaks corresponding to crystalline sulfur (JCPDS 01-078-0188), confirming the successful incorporation and retention of sulfur in its crystalline form across all synthesis routes. The XRD pattern of pristine AB reveals two broad peaks at approximately 23° and 44°, attributed to the (002) and (100) planes of disordered graphitic carbon, respectively. These features remain present in the composites, indicating that the structural framework of AB is preserved during synthesis. A closer examination of the sulfur peak intensities showed notable differences between the four methods, with BM and ChP composites exhibiting sulfur peaks that were approximately 10 times more intense than those for DC and MD composite materials. It is important to note that the intensity scale for BM and ChP was adjusted (multiplied by a factor of 10) in Fig. 1b to allow meaningful visual comparison. This notable contrast in peak intensity is possibly due to a larger fraction of sulfur residing either on the external surface or weakly attached to the carbon framework,[67] while for DC and MD, the smaller sulfur particles are infused into the pores of the AB matrix.[68]

The low-temperature N_2 adsorption–desorption isotherms of the AB@S composites (Fig. 1c) correspond to a type IV isotherm with H3-type hysteresis loops at high relative pressures (P/P_0 > 0.8), as classified by IUPAC.[69] This behavior is indicative of mesoporous structures and capillary condensation within mesopores. The presence of these features confirms that the porosity of the AB matrix is largely retained after sulfur incorporation, although its characteristics vary depending on the synthesis route. Among the samples, composites prepared *via* BM and MD exhibit the highest adsorption volumes at elevated P/P_0, reflecting a greater total pore volume (Fig. 1d) and more developed porous structures. BET analysis reveals a clear trend of decreasing specific surface area and increasing average pore size following sulfur immobilization, due to pore filling by sulfur. Pristine AB exhibited a surface area of 76.7 $m^2\ g^{-1}$, an average pore size of 11 nm (Table S2). After sulfur incorporation, these values declined significantly across all samples (Fig. S2), with the most pronounced decrease observed for composites synthesized *via* ChP and MD, which displayed surface areas of only 7.3 $m^2\ g^{-1}$ and 9.8 $m^2\ g^{-1}$, respectively. In contrast, the BM and DC composites retained relatively higher surface areas of 16.1 $m^2\ g^{-1}$ and 16.2 $m^2\ g^{-1}$, suggesting incomplete pore filling or partial sulfur dispersion. These two samples also exhibited the highest total pore volumes, ranging from 0.063 to 0.074 $cm^3\ g^{-1}$ (Table S2). Pore size distributions calculated by the BJH

method confirm that all AB@S composites maintain mesoporous character (2–50 nm), with average pore widths spanning from 9 to 16 nm. The BJH desorption pore widths also differed among the AB@S. The ChP composite had 24.2 nm, while MD and DC had 19.4 nm and 20 nm, respectively. The BM composite displayed the smallest pore width of 18.9 nm. This smaller value suggests efficient sulfur encapsulation within fine mesopores. Besides, this smaller pore size contributes to the higher sulfur evaporation endpoint observed in the TGA profile of BM.[70] These structural features are of particular importance for Li–S battery applications. The high surface area enables efficient sulfur reduction into Li_2S, while the presence of interconnected mesopores and sufficient pore volume is crucial for accommodating sulfur, facilitating lithium-ion transport, and mitigating polysulfide dissolution.[71] Therefore, the observed differences in porosity and surface area among the composites may have a direct impact on their electrochemical behavior and long-term cycling stability.

Raman spectroscopy (Fig. 2) provides further insight into the structural and compositional characteristics of the AB@S composites. The spectra display two prominent bands: the D band at about 1340 cm^{-1}, associated with disordered carbon (sp^3 hybridization), and the G band at about 1578 cm^{-1}, corresponding to graphitic carbon (sp^2 domains). However, the shift of the G band in the DC composite toward a lower wavenumber (1550 cm^{-1}) compared to other samples indicates possible lattice stretching of the carbon framework or the presence of double bonds that resonate at lower frequencies.[72] After sulfur immobilization, the intensity ratio of the D-band to G-band (I_D/I_G), related to the degree of disorder or defects in the carbon structure, decreases from 1.096 for AB due to sulfur distribution within pores. Similar trends have been reported in previous studies, where a decrease in the I_D/I_G ratio after sulfur incorporation was also observed, confirming that sulfur impregnation into the pores can reduce the defect density of the carbon framework and increase structural ordering.[73,74] The ratio is highest for the AB@S composite by BM and equals 1.034 (Fig. 2b) and the lowest for the MD composite (Fig. 2d), suggesting fewer defects in the structure. The higher degree of structural disorder in the BM sample can be explained by the high-energy mechanical treatment during the BM process, which is able to introduce defects into the carbon structure, particularly at the edges.[66] The presence of defects and active sites in the BM composite also ensures better polysulfide trapping and electrochemical performance.[63,66] For the ChP sample, the mild chemical precipitation conditions do not induce the same level of structural defects as observed for BM,[75] while the thermal methods, such as MD and DC, do not provide sufficient defect generation in the AB matrix. Together, the XRD and Raman analyses provide clear evidence that all four immobilization techniques successfully incorporate sulfur into the AB matrix, but they differ in terms of sulfur crystallinity and interaction with the carbon support, factors that may critically influence the resulting electrochemical performance.

The morphology and microstructure of AB and the synthesized AB@S composites were examined using scanning electron microscopy (SEM) and transmission electron microscopy (TEM). SEM images of pristine AB (Fig. S3) and AB@S composites (Fig. 3) reveal insights into particle shape and distribution. Across all samples, spherical particles with

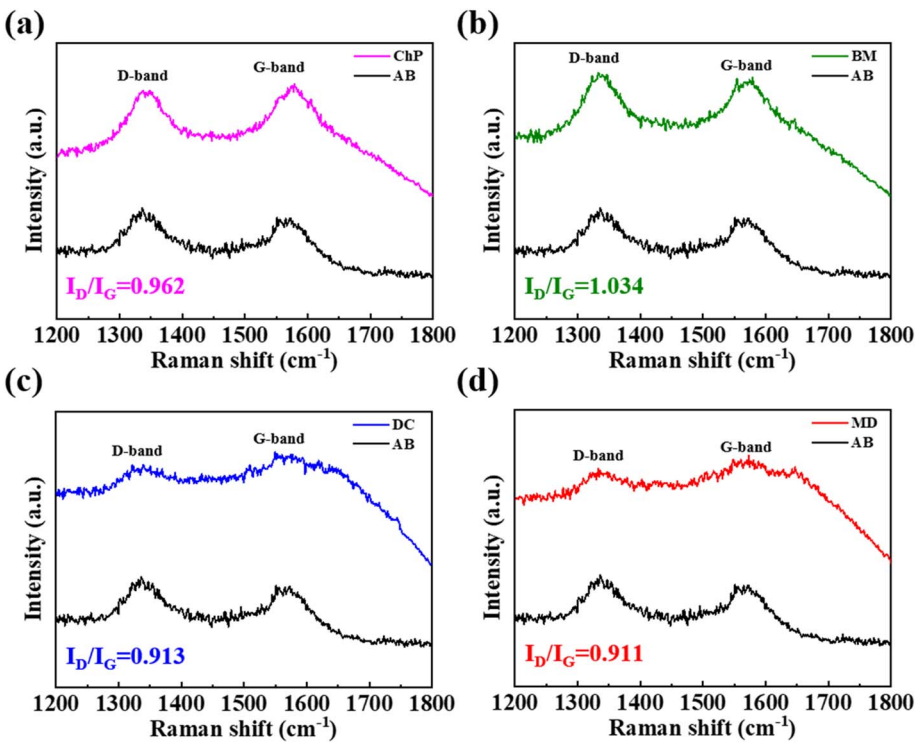

Fig. 2 Raman spectrum of AB@S cathode materials (a) by ChP; (b) by BM; (c) by DC, and (d) by MD.

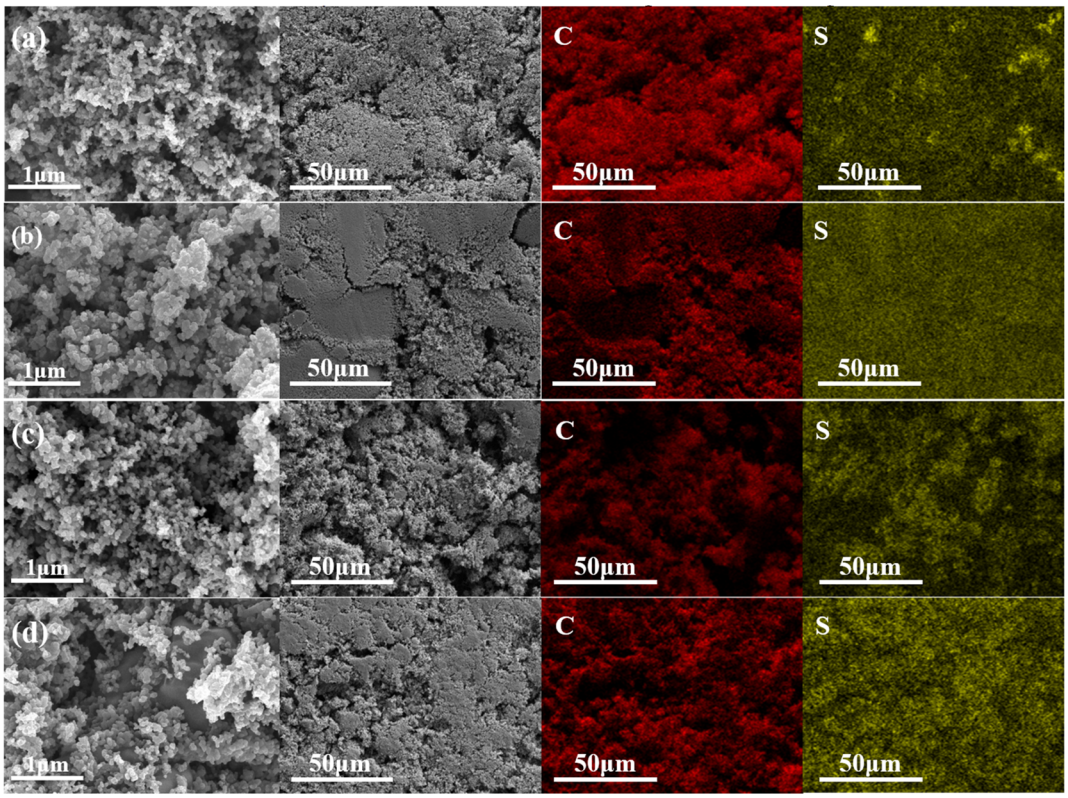

Fig. 3 SEM and EDS mapping of AB@S obtained (a) by ChP; (b) by BM; (c) by DC, and (d) by MD.

nanometer-scale dimensions (~100 nm) are observed. Notably, the composites obtained *via* ChP and DC methods exhibit a well-developed porous structure, which is favorable for sulfur hosting. In contrast, the BM method results in the formation of bigger sulfur–carbon particle aggregates, likely due to mechanical compaction during high-energy milling. The MD sample shows moderate agglomeration, though to a lesser extent than the BM sample. These morphological differences reflect the influence of each synthesis method on sulfur dispersion and composite architecture.

To further investigate the distribution of sulfur and carbon within the AB@S composites, EDS mapping was performed (Fig. 3). The EDS elemental maps provide detailed insights into the homogeneity of carbon (C) and sulfur (S) across the different samples. The composite synthesized *via* the BM method exhibits the most uniform and finely dispersed sulfur distribution, due to the strong mechanical forces involved in the milling process, which effectively break down sulfur particles and embed them into the porous carbon matrix. The MD sample similarly demonstrates homogeneous sulfur dispersion, with minimal aggregation, indicating efficient sulfur infiltration into the porous structure. In the case of the ChP method, sulfur is relatively well-distributed on the surface of the AB particles; however, localized sulfur agglomerates are present, which may reduce active material utilization. The DC composite displays a coarser morphology with evenly distributed sulfur and small, fused particle clusters.

The TEM images in Fig. 4 provide detailed insight into the microstructure of the AB@S cathode material. Similar to pure AB (Fig. S4), a distinctive chain-like arrangement of AB nanoparticles is observed within the sulfur matrix, forming interconnected pathways that facilitate efficient electron flow.[76] This structure is beneficial for improving the electrical conductivity of the composite, as it allows for rapid electron transport across the material.[65] Upon closer inspection, the TEM images reveal fine sulfur particles (dark particles) uniformly dispersed on the

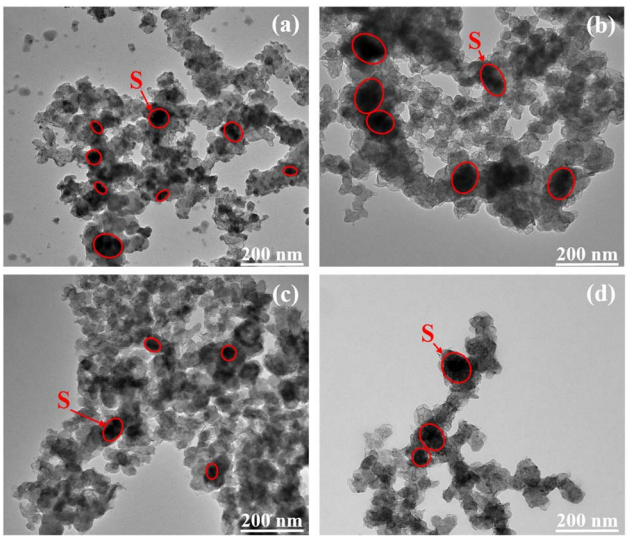

Fig. 4 TEM images of AB@S cathode materials obtained (a) by ChP; (b) by BM; (c) by DC, and (d) by MD.

carbon surface (gray particles). Besides, the analysis revealed a greater number of sulfur particles visible in the ChP and BM samples (Fig. 4a and b), indicating their presence on the surface of the carbon matrix, especially a lot in the ChP composite, while DC and MD methods effectively encapsulated sulfur into the pores of carbon.[57] This finding is also confirmed by the XRD patterns, which exhibit more intense peaks in the ChP and BM samples. Thus, in the BM composite, sulfur is located both inside the pores of the carbon and on its surface. Together, the TEM and XRD results collectively indicate that the degree of sulfur confinement within the porous carbon host varies significantly with the immobilization techniques.

3.2 Electrochemical performance of the AB@S cathode materials obtained by different sulfur immobilization methods

The electrochemical behavior of the AB@S electrodes was evaluated using CR-2032-type coin cells. Fig. 5 shows the CV profile of AB@S cells by ChP, BM, DC, and MD obtained at the scan rate of 0.1 mV s^{-1} within the voltage range of 1.6–2.8 V. All four electrodes display two reduction peaks at approximately 2.3 V and 2.0 V. The first cathodic peak at 2.3 V corresponds to the reduction of elemental sulfur to long-chain LiPSs (Li_2S_8/Li_2S_4), while the second represents the further reduction of polysulfides to insoluble Li_2S_2/Li_2S. The broad anodic peak near 2.4 V is attributed to the reverse oxidation of Li_2S/Li_2S_2 back to long-chain polysulfides and eventually elemental sulfur. Comparing electrodes on the first cycle, the DC cathode demonstrates the smallest potential gap between the reduction and oxidation peaks, suggesting lower polarization.[70] Besides, DC and MD electrodes have sharper peaks, showing higher electrochemical activity[77] and faster kinetics of lithium sulfur formation.[75] However, the MD cell demonstrates the largest potential gap and hence, increased polarization. The BM and ChP cathodes exhibit moderate redox performance on the first cycle, indicating balanced but less pronounced electrochemical kinetics compared to DC.

The CV over five consecutive cycles was also used to evaluate the electrochemical stability and reversibility of the four cathodes (Fig. S5). Notably, the DC cathode's oxidation peaks gradually decrease and shift toward higher potential during cycling (Fig. S5c), suggesting increased polarization and a decline in redox kinetics over time. Similarly, the MD electrode displays a noticeable loss in peak intensity and consistent potential shifts, indicating a loss of active material and decreasing capacity. In both cases, the lack of significant peak overlap across cycles points to limited electrochemical stability and reduced reversibility, despite promising initial performance. In contrast, the BM cell showed the best degree of overlap (Fig. S5b), denoting excellent stability, high redox reversibility, and effective "shuttle effect" mitigation. The minimal changes in peak shape, intensity, and position also suggest that sulfur was homogeneously infiltrated into AB pores.[75] The ChP electrode ranked second in terms of stability, demonstrating similarly good performance, though with a distinct drop in peak intensity between the first and second cycles. This behavior is likely associated with electrolyte wetting during the first cycle, after which the electrode stabilizes.

The cycling performance of AB@S cathodes at a current rate of 0.1C is depicted in Fig. 6a. To ensure an accurate comparison, the sulfur content of the composites was first evaluated by TGA. The analysis confirmed that all samples contained 70 ± 2.4 wt% of sulfur. To minimize the effect of small variations, the specific capacity values were normalized to the actual sulfur content of each composite. The areal sulfur loading of the electrodes was in the range of 1.0–1.13 mg cm^{-2}, thereby ensuring a comparable evaluation. The results show that the cell with the ChP cathode exhibits the highest initial discharge capacity of 948 mAh g^{-1}, which significantly decreases during the first few cycles. After 100 cycles, the value drops to 443.89 mAh g^{-1}, retaining only 55% of the initial discharge capacity, if calculated from the third cycle. The coulombic efficiency is also relatively low, averaging around 75%. The rapid decline may be attributed to the uneven distribution of sulfur and the formation of agglomerates, as well as the presence of sulfur mainly on the carbon surface, so it is easily dissolves in the electrolyte, causing rapid active material loss, low coulombic efficiency, and capacity fading.[78] On the contrary, the BM-derived cathode shows the best performance retention at 68%, decreasing from 798 mAh g^{-1} in the third cycle to 549 mAh g^{-1} after 100 cycles. The discharge capacities for MD and DC cells is retained at around 60%, falling to 480.15 mAh g^{-1} and 422.13 mAh g^{-1}, respectively. The coulombic efficiency of BM, DC, and MD approaches 99% during charge–discharge cycling. The galvanostatic charge–discharge profile (Fig. 6b) for the 10th cycle of the cell with ChP, BM, DC, and MD cathodes at 0.1C displayed a charge plateau at around 2.4 V and two reduction plateaus at about 2.3 V and 2 V, consistent with the CV measurements. The BM cell shows a promising discharge capacity of 810 mAh g^{-1}, unlike ChP, DC, and MD cells that display 630, 582, and 669 mAh g^{-1}, respectively. Besides, the smallest potential gap between the charge–discharge plateaus in the BM cell (215 mV) indicates less polarization and improved kinetics, resulting in enhanced cycle stability and exceptional rate performance.[68] In contrast, the DC showed the largest potential gap (263 mV) by the 10th cycle, although it initially exhibited the smallest gap in

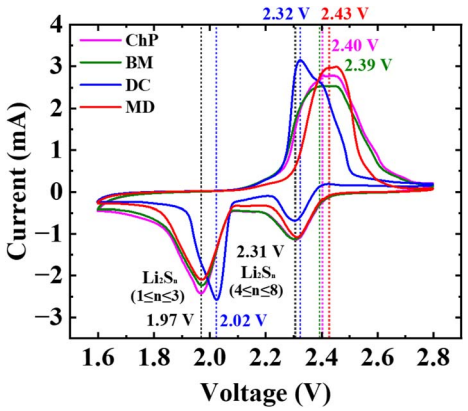

Fig. 5 CV curves of AB@S cathode obtained by ChP, BM, MD, and DC methods.

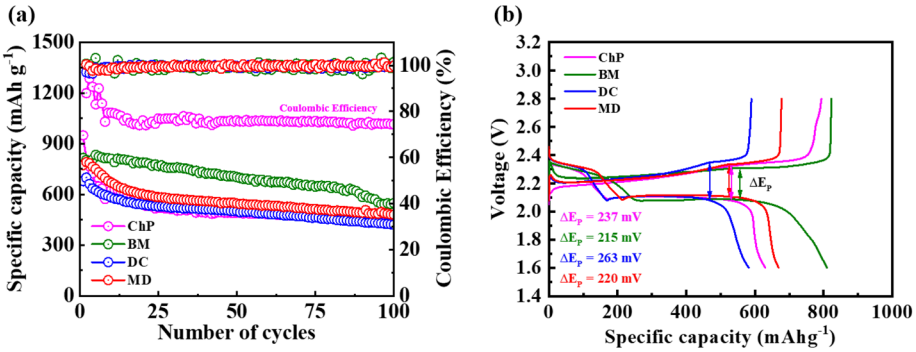

Fig. 6 (a) Cycling performance at 0.1C current rate of the AB@S cathodes; (b) galvanostatic discharge/charge curves in the 10th cycle of the cathodes with sulfur loading of 1.0–1.13 mg cm^{-2} at 0.1 C.

the CV measurements, suggesting worsening electrode kinetics and increased polarization over cycling. To put our work in context, previous studies have also evaluated AB-based sulfur cathodes for their electrochemical performance, as summarized in Table S3. Although these investigations focused on individual composites rather than a direct comparison of sulfur immobilization methods, our results fall within – or in some cases surpass – the ranges reported, supporting the reliability and relevance of our findings.

The rate performance of the cells was evaluated by measuring the discharge capacities at various current densities (0.1, 0.2, 0.5, and 1C). As shown in Fig. 7a, at a current rate of 0.1C, the BM cell exhibited the highest initial discharge capacity of 802 mAh g^{-1}, followed by DC at 754 mAh g^{-1}, ChP at 708 mAh g^{-1}, and MD at 705 mAh g^{-1}. However, as the current rate increased, the performance trends changed. The BM sample maintained relatively stable capacities across all current densities, demonstrating good rate capability. The uniform sulfur distribution in the carbon matrix achieved by the BM composite ensures good contact between sulfur and AB, and hence, lower charge transfer resistance and enhanced electronic conductivity of the electrode,[68,75,79] while partially defected carbon with a large surface area facilitates rapid Li^+ transport by providing abundant active sites and shortened diffusion pathways.[66] However, the limited capacity recovery of the BM cell suggests the dominance of irreversible degradation mechanisms. The BM cell only recovered to 536 mAh g^{-1} at 0.1C, corresponding to a permanent loss of 33% from its initial value. In contrast, both MD and DC showed better recovery behavior, with capacities rebounding to 635 mAh g^{-1} at the final 0.1C step. The cathode structure and sulfur confinement remain sufficiently stable after the heat treatment, which enables the capacity values to successfully recover to high levels. However, the DC sample delivered a significantly lower capacity at high current rates, reaching approximately 350 mAh g^{-1} at 1C. Possibly, the DC sample sulfur is more deeply embedded into the pores compared to the MD sample, so the electrochemical reactions become strongly diffusion-limited at high current rates. The ChP sample exhibited the poorest rate performance, with a sharp capacity drop to 454 mAh g^{-1} at 0.2C and further down to 303 mAh g^{-1} at 1C. Its capacity recovery was also the lowest, achieving only 487 mAh g^{-1} when switching back to 0.1C. The weak confinement and large crystalline sulfur aggregates in the composite formed by ChP are prone to polysulfide dissolution and rapid loss of active material, leading to the active drop in capacity.

Besides, the EIS measurements were carried out for cells before cycling between 100 kHz and 10 mHz. Fig. 7b shows Nyquist plots of AB@S cathodes prepared by four methods. The semicircle indicates the charge transfer resistance (R_{ct}), generated at the electrode–electrolyte interface, while a straight line in the low-frequency region is attributed to Warburg impedance (W), arising due to the diffusion of Li^+ ions within the electrode.[60,76] Comparing the cells, the R_{ct} value for MD is the

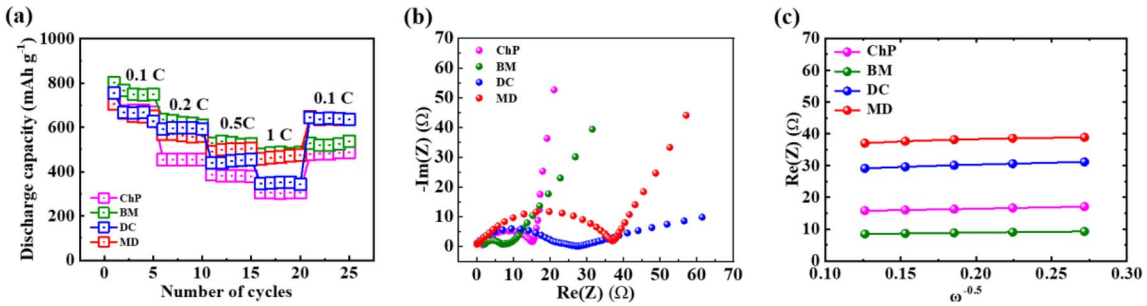

Fig. 7 (a) Rate performance, (b) EIS curves of the cells with AB@S cathodes prepared by four different methods, and (c) the linear figure of Re(Z) at $\omega^{-0.5}$.

highest (37 Ω), then DC, ChP, and BM cells experience 27, 15, and 7 Ω, respectively, indicating that the BM electrode has a good electrolyte penetration and enhanced reaction kinetics. This can be attributed to the more uniform sulfur distribution, as evenly distributed sulfur promotes charge and electron transfer.[76]

To compare the lithium-ion diffusion coefficients of four methods among the sulfur immobilization methods, the low-frequency region of the EIS spectra was analyzed.

$$Z_{re} = R_s + R_{ct} + \sigma_w \omega^{-0.5} \quad (1)$$

Eqn (1) establishes the linear dependence of Re(Z) on $\omega^{-0.5}$ in the low-frequency region, as illustrated in Fig. 7c, where the slope corresponds to the Warburg coefficient (σ, Ω $s^{0.5}$). This parameter is then used in eqn (2) to calculate the lithium-ion diffusion coefficient (D).[80–83]

$$D = \frac{R^2 T^2}{2A^2 N^4 F^4 C^2 \sigma_W{}^2} \quad (2)$$

where R is the gas constant (8.314 J mol^{-1} K^{-1}); T is the absolute temperature (298 K); A is the surface area of the electrode (A = 1.77 cm^2); N is the number of electrons involved in the redox reaction (N = 2); F is Faraday's constant (96 485C mol^{-1}); C is the concentration of the lithium ions in the electrolyte (C = 1.28 mol L^{-1}).

The corresponding impedance parameters and D values are summarized in Table 1. Among the samples, the BM cathode demonstrated the lowest total resistance (7 Ω) and smallest σ (5.587 Ω $s^{0.5}$), resulting in the highest diffusion coefficient (1.39 × 10^{-11} m^2 s^{-1}). By contrast, DC and MD showed significantly larger resistances and σ values, leading to much lower D (2.27 × 10^{-12} and 2.80 × 10^{-12} m^2 s^{-1}, respectively). The ChP electrode displayed intermediate behavior with a D of 5.56 × 10^{-12} m^2 s^{-1}. These results demonstrate that the BM method favors more efficient lithium-ion transport at the electrode/electrolyte interface, consistent with its improved cycling performance at moderate rates, while the lower D values of ChP, DC, and MD imply sluggish ion transport that limits their electrochemical behavior.

As visualized in the radar chart (Fig. 8), the BM method exhibits the most favorable combination of synthesis and electrochemical characteristics. For clarity, the synthesis parameters in the radar chart were defined as follows: sulfur immobilization ability – the degree of sulfur retention in the carbon matrix, calculated as the match between actual sulfur loading from TGA and the theoretical stoichiometry; sulfur immobilization time – the duration required for sulfur incorporation into the carbon host (several hours for BM and ChP, 12–15 hours heating for DC and MD); composite porosity – the BET surface area, reflecting the pore volume and accessibility for sulfur and electrolyte; and sulfur distribution homogeneity – the uniformity of sulfur dispersion in the composite, evaluated by EDS mapping. The electrochemical parameters included coulombic efficiency (ratio of discharge to charge capacity per cycle, indicating reaction reversibility), charge transfer conductance (inverse of charge transfer resistance from EIS, with higher values indicating better conductivity), performance at different current rates (capacity retention under various C-rates and recovery after high-rate cycling), initial discharge capacity (third-cycle capacity at low rate), and capacity retention (capacity after prolonged cycling, normalized to the value at the third cycle). All parameters were scaled on a 0–10 range, with higher values corresponding to better performance, and the concentric circles in the radar chart indicate relative levels: Low (inner), Medium (middle), and High (outer).

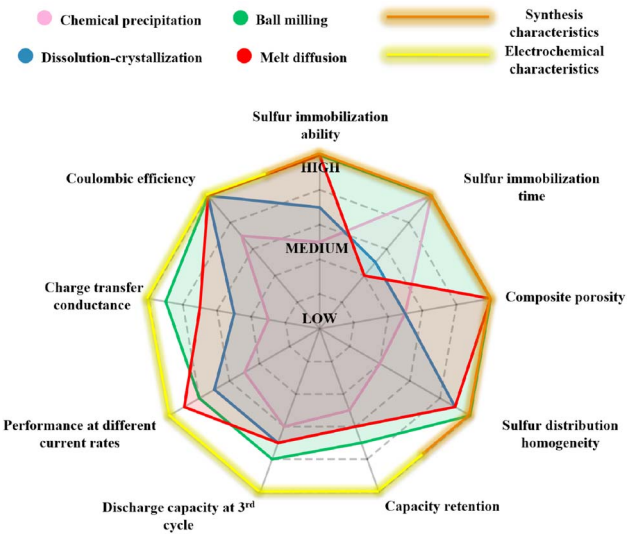

Fig. 8 Comparative radar chart of synthesis parameters and corresponding electrochemical characteristics for sulfur immobilization methods.

The BM immobilization method ranks high in uniform sulfur distribution, capacity retention, charge transfer conductance, and coulombic efficiency, reflecting its excellent sulfur confinement and stable cycling behavior. Additionally, the BM method achieves a strong initial discharge capacity and a moderate sulfur immobilization time, making it practical for

Table 1 Impedance parameters of the Li–S cells

Battery	(Resistance (R_{ct} + R_s)), Ω	Warburg coefficient (σ_w), Ω $s^{0.5}$	Diffusion coefficient (D), (m^2 s^{-1})
ChP	15	8.816	5.56 × 10^{-12}
BM	7	5.587	1.39 × 10^{-11}
DC	27	13.807	2.27 × 10^{-12}
MD	37	12.428	2.80 × 10^{-12}

scalable fabrication. While some methods outperform BM in isolated categories, for example, MD shows better performance at different current rates, BM stands out as the most balanced approach.

Beyond the laboratory-scale performance parameters, the BM approach also demonstrates several practical advantages that strengthen its relevance for industrial applications. According to literature reports, BM is widely recognized as a scalable, low-cost, and environmentally friendly technique for the preparation of sulfur–carbon composites.[47,66,84,85] All these attributes further support the BM method as a promising and practically feasible way for Li–S battery cathode fabrication.

4 Conclusion

In this study, four conventional sulfur infiltration methods – ChP, BM, DC, and MD – using AB as the traditional conductive carbon host were performed and compared. The results clearly demonstrate that the synthesis technique affects sulfur distribution, interaction with the carbon matrix, pore structure, and, consequently, the electrochemical performance of the resulting AB@S cathodes. Thus, the thermal analysis confirmed successful sulfur incorporation (~70 wt%) across all samples. Although ChP and DC required mass adjustments due to incomplete sulfur uptake, BM and MD methods ensured superior control on sulfur loading. Notably, the BM composite showed a delayed sulfur evaporation up to ~340 °C, suggesting strong sulfur confinement in pores, which can be attributed to the better incorporation of sulfur into the carbon matrix, and possible polysulfides formation. XRD and Raman spectroscopy confirmed the presence of crystalline sulfur and the disordered carbon structure across all composites, with the BM composite showing the highest I_D/I_G ratio due to the presence of defect-rich edges, which enhance polysulfide adsorption and electrochemical activity. Morphological studies further confirmed that the BM composite achieved exceptionally uniform sulfur dispersion, contributing to faster ion/electron transport and better electrode kinetics. The relatively high specific surface areas and total pore volumes of BM and DC composites and the smallest pore size in the BM composite ensure efficient sulfur confinement and effective prevention of polysulfide dissolution. During galvanostatic cycling at 0.1C, the BM cell demonstrated the best capacity retention (68%) and lowest charge–discharge plateau gap (215 mV) at the 10th cycle, outperforming ChP, DC, and MD cells. While the ChP method initially delivered the highest discharge capacity (948 mAh g^{-1}), it suffered from severe capacity fading due to sulfur agglomeration and high polysulfide dissolution, as reflected in its lower coulombic efficiency (75%). The DC and MD methods provided moderate results, demonstrating acceptable capacity retention of 60% but higher charge transfer resistance and lower initial discharge capacities. The rate performance at different scan rates further confirmed the excellent capacity of the BM cell at 0.1C, followed by a consistent decrease as the C-rate increases, although a moderate recovery after high-rate cycling. The BM cell also demonstrated moderate performance in CV, characterized by separated redox peaks and current intensities, and excelled in EIS, showing the lowest charge transfer resistance (7 Ω) and the most efficient lithium-ion transport.

Overall, the BM method stands out among other immobilization approaches due to its superior control and efficiency. It allows for easy and precise loading of sulfur, relying on expensive solvents or prolonged heating, unlike ChP and DC or MD. The relatively slow, but highly effective, mechanical action of the BM process ensures excellent sulfur distribution throughout the carbon matrix. Given that BM is already a well-established industrial process, this method is not only cost-effective and eco-friendly but also the most promising approach for sulfur cathode preparation in Li–S batteries.

Author contributions

Yelena Shinkarova: resources, investigation, methodology, data curation, writing – original draft, writing – review & editing; Malika Tyrsunbek: investigation, methodology, data curation; Mukhammed Kenzhebek: investigation, writing – review & editing; Batukhan Tatykayev: investigation, writing – review & editing; Zhazira Supiyeva: resources, funding acquisition; Temirlan Kerimkul: investigation; Fail Sultanov: conceptualization, methodology, validation, data curation, writing – review & editing, supervision; Almagul Mentbayeva: conceptualization, methodology, validation, supervision, writing – review & editing, project administration.

Conflicts of interest

The authors declare that they have no known competing financial interests or personal relationships that could have appeared to influence the work reported in this paper.

Data availability

The data supporting this article have been included as part of the SI and are available from the corresponding author upon reasonable request. Supplementary information is available. See DOI: https://doi.org/10.1039/d5ra05694b.

Acknowledgements

This research has been funded by the Committee of Science of the Ministry of Science and Higher Education of the Republic of Kazakhstan (grant no. BR27198045 and grant no. BR21882402).

References

1 D. A. Elalfy, E. Gouda, M. F. Kotb, V. Bureš and B. E. Sedhom, *Energy Strategy Rev.*, 2024, **54**, 101482.
2 K. C. Divya and J. Østergaard, *Elec. Power Syst. Res.*, 2009, **79**, 511–520.
3 T. Placke, R. Kloepsch, S. Dühnen and M. Winter, *J. Solid State Electrochem.*, 2017, **21**, 1939–1964.
4 J. Li, Z. Du, R. E. Ruther, S. J. An, L. A. David, K. Hays, M. Wood, N. D. Phillip, Y. Sheng, C. Mao, S. Kalnaus, C. Daniel and D. L. Wood, *JOM*, 2017, **69**, 1484–1496.

5 W. Ren, W. Ma, S. Zhang and B. Tang, *Energy Storage Mater.*, 2019, **23**, 707–732.
6 J. Wang, S. Yi, J. Liu, S. Sun, Y. Liu, D. Yang, K. Xi, G. Gao, A. Abdelkader, W. Yan, S. Ding and R. V. Kumar, *ACS Nano*, 2020, **14**, 9819–9831.
7 Q. Pang, X. Liang, C. Y. Kwok and L. F. Nazar, *J. Electrochem. Soc.*, 2015, **162**, A2567–A2576.
8 G. Li, S. Wang, Y. Zhang, M. Li, Z. Chen and J. Lu, *Adv. Mater.*, 2018, **30**, 1705590.
9 S. S. Zhang, *J. Power Sources*, 2013, **231**, 153–162.
10 H. Shi, W. Sun, J. Cao, S. Han, G. Lu, Z. A. Ghazi, X. Zhu, H. Lan and W. Lv, *Adv. Funct. Mater.*, 2023, **33**, 2306933.
11 P. Barai, A. Mistry and P. P. Mukherjee, *Extreme Mech. Lett.*, 2016, **9**, 359–370.
12 R. Fang, S. Zhao, Z. Sun, D. Wang, H. Cheng and F. Li, *Adv. Mater.*, 2017, **29**, 1606823.
13 D. M. Brieske, A. Warnecke and D. U. Sauer, *Energy Storage Mater.*, 2023, **55**, 289–300.
14 Z. W. Seh, Y. Sun, Q. Zhang and Y. Cui, *Chem. Soc. Rev.*, 2016, **45**, 5605–5634.
15 K. Fan and H. Huang, *Energy Storage Mater.*, 2022, **50**, 696–717.
16 A. Eftekhari and D.-W. Kim, *J. Mater. Chem. A*, 2017, **5**, 17734–17776.
17 Z. Wang, X. Xu, S. Ji, Z. Liu, D. Zhang, J. Shen and J. Liu, *J. Mater. Sci. Technol.*, 2020, **55**, 56–72.
18 Y. Chen, T. Wang, H. Tian, D. Su, Q. Zhang and G. Wang, *Adv. Mater.*, 2021, **33**, 2003666.
19 N. Yuan, Y.-R. Deng, S.-H. Wang, L. Gao, J.-L. Yang, N.-C. Zou, B.-X. Liu, J.-Q. Zhang, R.-P. Liu and L. Zhang, *Tungsten*, 2022, **4**, 269–283.
20 J. P. Zhu, X. H. Wang and X. X. Zuo, *R. Soc. Open Sci.*, 2019, **6**, 190634.
21 J. Huang and S. Dong, *Ionics*, 2022, **28**, 2775–2779.
22 X. Liu, J. Huang, Q. Zhang and L. Mai, *Adv. Mater.*, 2017, **29**, 1601759.
23 B. Ye, C. Feng, G. Zhu, S. Wang and A. Fakhri, *J. Alloys Compd.*, 2020, **823**, 153743.
24 L. Chen, X. Li and Y. Xu, *Funct. Mater. Lett.*, 2018, **11**, 1840010.
25 X. Chen, G. Du, M. Zhang, A. Kalam, S. Ding, Q. Su, B. Xu and A. G. Al-Sehemi, *Energ. Tech.*, 2020, **8**, 1901163.
26 B. Yuan, J. Zhao, W. Liu, H. Liu, P. Chen, L. Sun, X. Guo, X. Wang, W. Zhang, R. Zhang and F. Wang, *J. Alloys Compd.*, 2024, **987**, 174231.
27 H. Gamo, K. Hikima and A. Matsuda, *ACS Omega*, 2023, **8**, 45557–45565.
28 Q. Zhang, Q. Huang, S. Hao, S. Deng, Q. He, Z. Lin and Y. Yang, *Advanced Science*, 2022, **9**, 2103798.
29 H. Kang, H. Kim and M. J. Park, *Adv. Energy Mater.*, 2018, **8**, 1802423.
30 Z. Cheng, H. Pan, H. Zhong, Z. Xiao, X. Li and R. Wang, *Adv. Funct. Mater.*, 2018, **28**, 1707597.
31 K. Liu, H. Zhao, D. Ye and J. Zhang, *Chem. Eng. J.*, 2021, **417**, 129309.
32 X. Liang, A. Garsuch and L. F. Nazar, *Angew. Chem., Int. Ed.*, 2015, **54**, 3907–3911.
33 V. P. Nguyen, J. S. Park, H. C. Shim, J. M. Yuk, J. Kim, D. Kim and S. Lee, *Adv. Funct. Mater.*, 2023, **33**, 2303503.
34 Y. Liu, Y. Wang, C. Wang, J. Wang and J. Wang, *Carbon*, 2020, **167**, 930.
35 J. Zhang, Y. Wu, Y. Xing, Y. Li, T. Li and B. Ren, *J. Porous Mater.*, 2023, **30**, 1807–1819.
36 Y. Wang, B. Liu, W. Zhang, C. Shao, D. Lan, X. Qu, R. Chen, W. Zhang, W. Zhao, J. Liu, Y. Zhang and Z. Shi, *SN Appl. Sci.*, 2020, **2**, 1276.
37 Z. Li, X. Li, Y. Liao, X. Li and W. Li, *J. Power Sources*, 2016, **334**, 23–30.
38 W. Bao, Z. Zhang, W. Chen, C. Zhou, Y. Lai and J. Li, *Electrochim. Acta*, 2014, **127**, 342–348.
39 L. Zhang, R. A. Senthil, J. Pan, A. Khan, X. Jin and Y. Sun, *Ionics*, 2019, **25**, 4761–4773.
40 Q. Zhang, X. Cheng, J. Huang, H. Peng and F. Wei, *Carbon*, 2015, **81**, 850.
41 L. Huang, J. Li, B. Liu, Y. Li, S. Shen, S. Deng, C. Lu, W. Zhang, Y. Xia, G. Pan, X. Wang, Q. Xiong, X. Xia and J. Tu, *Adv. Funct. Mater.*, 2020, **30**, 1910375.
42 C. Wang, J. Chen, Y. Shi, M. Zheng and Q. Dong, *Electrochim. Acta*, 2010, **55**, 7010–7015.
43 Y. Sun, S. Wang, H. Cheng, Y. Dai, J. Yu and J. Wu, *Electrochim. Acta*, 2015, **158**, 143–151.
44 S. Li, H. Li, G. Zhu, B. Jin, H. Liu and Q. Jiang, *Appl. Surf. Sci.*, 2019, **479**, 265–272.
45 Z. Li, B. Wang, H. Su, Y. Shang and H. Liu, *Int. J. Electrochem. Sci.*, 2023, **18**, 100400.
46 M. R. Kaiser, J. Wang, X. Liang, H.-K. Liu and S.-X. Dou, *J. Power Sources*, 2015, **279**, 231–237.
47 J. Xu, J. Shui, J. Wang, M. Wang, H.-K. Liu, S. X. Dou, I.-Y. Jeon, J.-M. Seo, J.-B. Baek and L. Dai, *ACS Nano*, 2014, **8**, 10920–10930.
48 Y. Zhang, J. Ren, D. Wang, C. Zhang, F. Yin, A. Mukanova and Z. Bakenov, *Chemelectrochem*, 2018, **5**, 1591–1598.
49 S.-R. Chen, Y.-P. Zhai, G.-L. Xu, Y.-X. Jiang, D.-Y. Zhao, J.-T. Li, L. Huang and S.-G. Sun, *Electrochim. Acta*, 2011, **56**, 9549–9555.
50 X. Ji, K. T. Lee and L. F. Nazar, *Nat. Mater.*, 2009, **8**, 500–506.
51 Y.-S. Su and A. Manthiram, *Electrochim. Acta*, 2012, **77**, 272–278.
52 W. Qin, B. Fang, S. Lu, Z. Wang, Y. Chen, X. Wu and L. Han, *RSC Adv.*, 2015, **5**, 13153–13156.
53 J. Li, N. Li, C. Li and Y. Guo, *J. Wuhan Univ. Technol.–Materials Sci. Ed.*, 2015, **30**, 10–15.
54 W. Yang, W. Yang, J. Feng and X. Qin, *J. Energy Chem.*, 2018, **27**, 813–819.
55 G. Liu, Z. Su, D. He and C. Lai, *Electrochim. Acta*, 2014, **149**, 136–143.
56 B. Zhang, Z. Guo, Y. Zhao, B. Luo, D. Li, T. Zhao, J. Sure, S. M. Vishnu, A. Abdelkader, C. Harris and K. Xi, *Electrochim. Acta*, 2021, **388**, 138650.
57 A. Manthiram, Y. Fu, S.-H. Chung, C. Zu and Y.-S. Su, *Chem. Rev.*, 2014, **114**, 11751–11787.
58 C. Ye, S. Xu, H. Li, J. Shan and S. Qiao, *Adv. Mater.*, 2024, 2407738.
59 S. Li and Z. Fan, *Energy Storage Mater.*, 2021, **34**, 107–127.

60 C. Jiao, C.-R. Zhao, L. Zhang, S.-Q. Zhao, G.-Y. Pang, H.-B. Sun and S.-G. Lu, *Rare Met.*, 2023, **42**, 3877–3885.
61 X. Geng, M. Rao, X. Li and W. Li, *J. Solid State Electrochem.*, 2013, **17**, 987–992.
62 J. H. Park, W. Y. Choi, J. Yang, D. Kim, H. Gim and J. W. Lee, *Carbon*, 2021, **172**, 624–636.
63 Á. Bonilla, A. Benítez, J. L. Gómez-Cámer and Á. Caballero, *J. Alloys Compd.*, 2023, **968**, 171810.
64 S. K. Cherian, K. Nanaji, B. V. Sarada, T. N. Rao and C. S. Sharma, *J. Energy Storage*, 2024, **89**, 111803.
65 M. Kazazi, F. Ghadami, M. R. Dadfar, M. Sobhani and A. H. Mohammadi, *Solid State Ionics*, 2016, **290**, 40–46.
66 W. Qin, S. Lu, Z. Wang and X. Wu, *J. Energy Chem.*, 2017, **26**, 448–453.
67 Y. Chen, H. Zhang, X. Yang, K. Feng, X. Li and H. Zhang, *RSC Adv.*, 2016, **6**, 81950–81957.
68 W. Yang, W. Yang, S. Di, G. Sun and X. Qin, *Curr. Nanosci.*, 2018, **14**, 335–342.
69 K. A. Cychosz, R. Guillet-Nicolas, J. García-Martínez and M. Thommes, *Chem. Soc. Rev.*, 2017, **46**, 389–414.
70 S. Wang, Z. Zhao, H. Xu, Y. Deng, Z. Li and G. Chen, *Electrochim. Acta*, 2015, **173**, 282–289.
71 T. Safdar and C. Huang, *RSC Adv.*, 2024, **14**, 30743–30755.
72 U. Gulzar, A. Lonergan, Y. Zhang, A. Grant, A. Carroll, M. Ferguson and C. O'Dwyer, *J. Electrochem. Soc.*, 2025, **172**, 010514.
73 J. Wang, Y. Liu, M. Cheng, H. Zhao, J. Wang, Z. Zhao, X. Duan, C. Wang and J. Wang, *Electrochim. Acta*, 2019, **318**, 161–168.
74 X. Zhao, J.-K. Kim, H.-J. Ahn, K.-K. Cho and J.-H. Ahn, *Electrochim. Acta*, 2013, **109**, 145–152.
75 T.-G. Jeong, J. Chun, B.-W. Cho, J. Lee and Y.-T. Kim, *Sci. Rep.*, 2017, **7**, 42238.
76 B. Zhang, C. Lai, Z. Zhou and X. P. Gao, *Electrochim. Acta*, 2009, **54**, 3708–3713.
77 G. Jin, Z. Mingang, Y. Shijian, Y. Xiaoyan and W. Shiwei, *Ionics*, 2018, **24**, 2219–2225.
78 L. Li, Z. Ma and Y. Li, *Carbon*, 2022, **197**, 200–208.
79 G. Li, W. Zhao, L. Liu and L. Chen, *RSC Adv.*, 2015, **5**, 54293–54300.
80 B. Li, C. Han, Y.-B. He, C. Yang, H. Du, Q.-H. Yang and F. Kang, *Energy Environ. Sci.*, 2012, **5**, 9595.
81 P. Xiao, Y. Cai, X. Chen, Z. Sheng and C. Chang, *RSC Adv.*, 2017, **7**, 31558–31566.
82 X. Qian, J. Cheng, L. Jin, J. Chen, Q. Hao and K. Zhang, *Colloids Surf., A*, 2023, **668**, 131442.
83 S. Zhao, Q. Hao, X. Qian, L. Jin, B. Li and H. Xu, *J. Energy Storage*, 2024, **101**, 113833.
84 Y. Zhang, K. Li, H. Li, Y. Wang, Y. Peng, S. Lin, B. J. Hwang and J. Zhao, *J. Alloys Compd.*, 2017, **729**, 331–337.
85 P. Xin, B. Jin, H. Li, X. Lang, C. Yang, W. Gao, Y. Zhu, W. Zhang, S. Dou and Q. Jiang, *Chemelectrochem*, 2017, **4**, 115–121.